COBEM 2023 27TH INTERNATIONAL CONGRESS OF MECHANICAL ENGENEERING

ABCM Brazilian Society of Mechanical Sciences and Engineering
27th ABCM International Congress of Mechanical Engineering
December 04-08, 2023, Florianópolis-SC, Brazil

COB-2023-0240
ON THE MECHANICS OF RUPTURED AND UNRUPTURED INTRACRANIAL ANEURYSMS: NUMERICALLY ASSESSING HOW DIFFERENT PROPERTIES MAY AFFECT THEIR MECHANICAL BEHAVIOR

Iago Oliveira
São Paulo State University (UNESP), School of Engineering, Bauru, São Paulo, Brazil
iago.oliveira@unesp.br

Carlos Eduardo Baccin
Interventional Neuroradiologist, Hospital Israelita Albert Einstein, São Paulo, Brazil
cebaccin@gmail.com

José Luiz Gasche
São Paulo State University (UNESP), School of Engineering, Ilha Solteira, São Paulo, Brazil
jose.gasche@unesp.br

Abstract. *Intracranial aneurysms (IAs), a dangerous disease with up to 50 % mortality rate in case of rupture, is characterized as a dilatation of the cerebral arteries, most commonly occurring in the form of a sac. Biologically, their walls fit within the class of soft tissues. Numerical studies using patient-specific IA geometries have become increasingly popular as a tool to better understand the mechanics of the disease and, most pressing, to potentially help predict a rupture event. To that end, the mechanical properties of the tissue have to be known. Although these data are relatively scarce, recent experimental studies suggest that the mechanical properties of ruptured and unruptured aneurysms differ significantly. Consequently, it indicates that their mechanical behavior might be different. In this context, we compared the mechanical response, computed numerically, between ruptured and unruptured cases of patient-specific IAs. Pulsatile numerical simulations were carried out in twelve patient-specific IAs geometries using the one-way fluid-solid interaction solution strategy implemented in solids4foam, in which the blood flow is solved and its traction field is applied as the driving force of the wall motion. The IA and artery walls were assumed isotropic and their thickness and material properties were computationally created with a modeling in which these properties were assumed uniform over the aneurysm sac. Additionally, we used experimental data of ruptured and unruptured IA samples to obtain the mechanical constants for the Mooney-Rivlin law that was used to model the tissue constitutively. We found that the stress levels in the IAs sacs were not significantly different between the ruptured and unruptured groups. Actually, the stress levels were slightly higher on unruptured aneurysms. On the other hand, the ruptured IAs had a significantly higher maximum stretch compared to unruptured ones. This indicates that deformation-related properties of the wall may indicate rupture and, thus, may serve as a proxy parameter to indicate a possible rupture event.*
Keywords: *intracranial aneurysms, wall mechanics, rupture status,* `solids4foam`*, numerical analysis*

1. INTRODUCTION

Intracranial aneurysms (IAs) are pathological dilatations in the vascular system occurring in the arteries that reach the brain, more commonly found in the bifurcations of that vascular tree, but also laterally to those arteries. It is a dangerous disease with up to 50 % mortality rate in case of rupture (Vlak *et al.*, 2013; Saqr *et al.*, 2019). The rupture event is hard to predict and currently available treatments also pose risk to patients, leaving physicians with a tough decision about whether to treat or not a particular patient. Hence, more reliable metrics to predict the rupture event have occupied researchers for the past two decades and a possible path to find those metrics is to understand the progression of the disease leading to the rupture. Part of that research on the subject employed numerical tools, such as Computational Fluid Dynamics (CFD) (Liang *et al.*, 2019), because it is widely accepted today that IAs are acquired lesions related to the interaction between the hemodynamic environment in the aneurysm lumen and its wall. Currently, the practical use of numerical techniques to assess the likelihood of IA rupture is a debated topic in the literature (Kallmes, 2012; Cebral and Meng, 2012).

Although the majority of the works involving CFD simulations in aneurysms geometries focused solely on the hemodynamics, a growing number of works is interested on the Fluid-Solid Interaction (FSI) between the blood flow and the

wall motion, which allows to predict the stresses and strain in the wall of a patient-specific IAs. This approach can provide valuable information to add in the decision process of neurosurgeons, such as the stresses in the wall, because, ultimately, the rupture occurs in the wall, and hence, from a material perspective, it may occurs when the stresses in the wall exceeds the strength of the tissue. However, when modeling an IA wall tissue, a difficulty is the lack of patient-specific data of the wall morphology, such as its thickness, and mechanical properties.

Recent studies have provided population-averaged data on the mechanical properties of intracranial aneurysm tissue. Robertson *et al.* (2015), for example, compared the mechanical response of cerebral arteries and IAs tissue samples by performing uniaxial traction tests with 15 rectangular strips from the meridional section of unruptured IAs and 12 circumferential samples of arteries of the circle of Willis extracted from human cadavers. The authors found that the tissue of intracranial arteries is typically stiffer than IAs tissue. In another study, Costalat *et al.* (2011), using uniaxial stress tests, found that unruptured IA tissue is stiffer than ruptured tissue. Moreover, their results suggest that the tissue becomes increasingly soft as the aneurysm progresses towards rupture. Additional studies further support the aforementioned findings (Brunel *et al.*, 2018).

This variability in the mechanical properties of IAs, compared with intracranial arterial tissue, or among aneurysms with different rupture status may impact the values of stresses and stretches in their wall. Particularly, it remains broadly unknown what is the effect of using different material properties on the mechanical response of IAs, especially due to their complex three-dimensional geometry. Therefore, the aim of this work is to assess the impact of different mechanical properties of ruptured and unruptured IAs on their mechanical response by using numerical simulations of the fluid-solid interaction between blood flow and the wall motion. To this end, we have employed recently acquired experimental data on the mechanical properties of IA tissue (Costalat *et al.*, 2011; Brunel *et al.*, 2018).

2. NUMERICAL METHODOLOGY

2.1 Sample Selection and Geometry Preparation

We selected twelve vascular geometries from digital subtraction angiography (DSA) examinations collected retrospectively and harbouring thirteen bifurcation IAs, all of them originating from the internal carotid artery (ICA) and middle cerebral artery (MCA). Nine cases were collected at the Albert Einstein Israelite Hospital, São Paulo, Brazil. Their use was approved by the Research Ethics Committees of the Albert Einstein Israelite Hospital, São Paulo, Brazil, and of the São Paulo State University (UNESP), Brazil, where the study was conducted. Furthermore, due to a lack of sufficient ruptured cases in the original dataset, three additional vascular geometries were obtained from the Aneurisk dataset repository (Passerini, T. and Piccinelli, M. and Veneziani, A. and Antiga, L., 2021) (available under the "CC BY-NC 3.0" license).

The images were segmented using the Vascular Modeling Toolkit (VMTK)® library (VMTK, 2022) with the level-sets method (Piccinelli *et al.*, 2009) by selecting a region of interest that encloses only an aneurysm and its surrounding vessels. Then, a triangulated surface was generated with the Marching Cubes algorithm (Antiga *et al.*, 2002, 2008), and inlet and outlet profiles were opened on it to impose boundary conditions for the numerical simulations. Seven IAs were unruptured, and six were ruptured. In this text, we label these images by appending their rupture status, prefix "r" for ruptured and "ur" for unruptured, to their parent artery. For example, a ruptured case in the ICA bifurcation is labeled "rICA", followed by a natural number in case of repetition.

2.2 Physical and Mathematical Modeling

We employed the so-called "one-way fluid-solid interaction (1WFSI)" strategy to numerically solve for the interaction between the blood flow and the solid wall motion (Hirschhorn *et al.*, 2020). By using this technique, the pulsatile fluid flow is solved by assuming a rigid FSI interface, i.e. with zero mass flux, zero pressure gradient, and the no-slip condition. Then, at each instant in time along the cardiac cycle, the traction on this interface due to the blood flow is transferred to the solid FSI interface counterpart and applied as a traction boundary condition. The resulting solid deformation is not transferred back to the fluid domain.

Blood was assumed to be a weakly compressible Newtonian fluid flowing in an isothermal laminar regime, therefore with governing equations given by the continuity equation:

$$\frac{\partial}{\partial t}\left(\int\limits_{V^{\mathrm{f}}} \rho^{\mathrm{f}}\,\mathrm{d}V\right) + \oint\limits_{S^{\mathrm{f}}} \rho^{\mathrm{f}}\boldsymbol{v}^{\mathrm{f}} \bullet \boldsymbol{n}^{\mathrm{f}}\,\mathrm{d}S = 0\,, \tag{1}$$

where $\boldsymbol{v}^{\mathrm{f}}$ is the flow velocity, ρ^{f} is the blood density, and $\boldsymbol{n}^{\mathrm{f}}$ is the outward normal vector to the control surface S^{f} of the

control volume V^{f}; and the momentum equation:

$$\frac{\partial}{\partial t}\left(\int\limits_{V^{\mathrm{f}}} \rho^{\mathrm{f}}\boldsymbol{v}^{\mathrm{f}}\mathrm{d}V\right) + \oint\limits_{S^{\mathrm{f}}} \rho^{\mathrm{f}}\boldsymbol{v}^{\mathrm{f}}\boldsymbol{v}^{\mathrm{f}} \bullet \boldsymbol{n}^{\mathrm{f}}\mathrm{d}S = \oint\limits_{S^{\mathrm{f}}} \boldsymbol{\sigma}^{\mathrm{f}} \bullet \boldsymbol{n}^{\mathrm{f}}\mathrm{d}S\,, \tag{2}$$

where $\boldsymbol{\sigma}^{\mathrm{f}}$ is the Cauchy stress tensor, given by:

$$\boldsymbol{\sigma}^{\mathrm{f}} = -p^{\mathrm{f}}\boldsymbol{I} + \mu\left[\nabla\boldsymbol{v}^{\mathrm{f}} + (\nabla\boldsymbol{v}^{\mathrm{f}})^{\mathrm{T}}\right] - \frac{2}{3}\mu\left(\nabla \bullet \boldsymbol{v}^{\mathrm{f}}\right)\boldsymbol{I}\,, \tag{3}$$

with p^{f} being the flow pressure and $\boldsymbol{I}$ the second-order identity tensor and blood dynamic viscosity assumed to be $\mu = 3.3 \times 10^{-3}\,\mathrm{Pa\,s}$. The compressibility of blood was assumed to be governed by the barotropic equation of state (Kanyanta, 2009), by which the pressure and the fluid density are linearly related through the equation:

$$\rho^{\mathrm{f}} = \rho_0^{\mathrm{f}} + \frac{\rho_0^{\mathrm{f}}}{\kappa^{\mathrm{f}}}\left(p^{\mathrm{f}} - p_0^{\mathrm{f}}\right)\,, \tag{4}$$

where κ^{f} is the bulk modulus of blood, assumed to be 2.2×10^9 Pa (Kanyanta, 2009) — measured early by Sacks and Tickner (1968), who found a similar value to the compressibility of water. The subscript "0" indicates a reference state of the fluid, assumed to be blood at a cardiac-cycle average pressure, 100 mmHg, with $\rho_0^{\mathrm{f}} = 1000.0\,\mathrm{kg/m^3}$.

Regarding the IA and artery wall motion, assumed in the finite-deformation regime, the momentum equation was solved in the total Lagrangian formulation that, in its integral form, is written as:

$$\int\limits_{V_0^{\mathrm{s}}} \rho_0^{\mathrm{s}}\frac{\partial^2\boldsymbol{u}}{\partial t^2}(\boldsymbol{\xi}, t)\mathrm{d}V_0 = \int\limits_{V_0^{\mathrm{s}}} \nabla_0 \bullet \left[J\boldsymbol{F}^{-1} \bullet (\boldsymbol{\sigma}^{\mathrm{s}} + \boldsymbol{\sigma}_0^{\mathrm{s}})\right]\mathrm{d}V_0\,, \tag{5}$$

where $\boldsymbol{\xi}$ indicates the coordinates system of the reference configuration, $\boldsymbol{u}$ is the wall displacement, ρ_0^{s} is the tissue density at the reference configuration, and $\boldsymbol{F} = \boldsymbol{I} + (\nabla_0\boldsymbol{u})^{\mathrm{T}}$ is the deformation gradient and $J = \det(\boldsymbol{F})$. In the solid properties, the subscript "0" indicates any property or derivative taken with respect to the reference configuration, assumed to be the domain configuration at the start of the cardiac cycle and with prestress given by $\boldsymbol{\sigma}_0^{\mathrm{s}} = J^{-1}\boldsymbol{F} \bullet \boldsymbol{S}_0 \bullet \boldsymbol{F}$. The second Piola-Kirchhoff prestress tensor, $\boldsymbol{S}_0$, was computed prior to solving each FSI simulation using the same approach employed by Bazilevs *et al.* (2010).

The wall tissue was assumed as isotropic and constitutively represented by the hyperelastic three-parameters Mooney-Rivlin law (Mooney, 1940) by using the pseudoelastic modeling approach (Fung *et al.*, 1979). Hence, the Cauchy stress of the wall tissue, $\boldsymbol{\sigma}^{\mathrm{s}}$, was calculated based on its strain-energy function, Ψ, as follows:

$$\Psi(I_1, I_2) = c_{10}\left(I_1 - 3\right) + c_{01}\left(I_2 - 3\right) + c_{11}\left(I_1 - 3\right)\left(I_2 - 3\right)\,, \tag{6}$$

where I_1 and I_2 are the first and second invariants of the right Cauchy-Green deformation tensor. The complete constitutive law employed a volumetric-decomposition approach Holzapfel *et al.* (2000). In this framework, the volumetric part of the tissue motion, dependent on the tissue compressibility, was ultimately measured by the Poisson's ratio of the tissue, ν^{s}, through its bulk modulus, κ^{s}, as given by the linearized elastic theory:

$$\kappa^{\mathrm{s}} = \frac{E}{3(1 - 2\nu^{\mathrm{s}})}\,, \tag{7}$$

where the linearized Young's modulus for the Mooney-Rivlin law was calculated based on the uniaxial deformation (given by $E = 6\left(\frac{\partial\Psi}{\partial I_1} + \frac{\partial\Psi}{\partial I_2}\right)$) (Holzapfel, 2000). We assumed a Poisson ratio of 0.48, which was defined after a parametric study of its influence on the stress and stretch on an IA sac surface. Values of ν^{s} closer to the incompressibility limit of $\nu^{\mathrm{s}} = 0.5$, changed the averaged stretch and stress fields on the sac by less than 1 % with the Mooney-Rivlin law.

All the details regarding the boundary conditions used for the solid and flow governing equations can be found in Oliveira *et al.* (2022). Briefly, at the inlet, the pressure gradient was set to zero and a time-varying populational-averaged pulsatile velocity profile was imposed based on the normalized flow rate reported by Hoi *et al.* (2010) for older adults — patient-specific blood flow rate waveforms at the ICA were not available. The velocity spatial profile was set according to the fully-developed laminar flow in a pipe — we attached an artificial circular-section extension, with a length equal to twice the diameter, to the artery inlet to impose this inlet flow condition. At the outlets, a flux-corrected velocity and a resistance boundary condition for pressure were imposed. The resistance boundary condition is defined as being proportional to the blood flow rate profile, but with levels ranging between the physiologically normal cardiac cycle pressure levels, i.e. from 80 to 120 mmHg (approximately 10 to 16 kPa). This boundary condition was recommended

by some reports showing that it is important to use it when the distances between the outlets and the aneurysm were not sufficiently long (Chnafa *et al.*, 2018) — we did not add cylindrical extensions at the outlets to avoid large computational meshes.

On the solid domain boundaries, a pressure of $p_o = 5\,\mathrm{mmHg}$, corresponding to the intracranial pressure, was imposed on its outer surface (Valencia *et al.*, 2013; Sanchez *et al.*, 2014). On the branches "sections" that were artificially created after the segmentation process, we imposed fixed zero displacements, or, mathematically, $\boldsymbol{u} = \boldsymbol{0}$. This decision was based on a comparison between the stress and displacement fields of three IA geometries computed with the zero-displacement and a "zero-shear" condition (Bazilevs *et al.*, 2010). The zero-displacement boundary condition did not influence the stress and stretch distributions on the IA sac when the artificial sections were created at least two local-arterial diameters from the aneurysm neck. This was assured for all geometries.

2.3 Wall Thickness and Material Constants Modeling

The detailed modeling of the wall thickness, e_w, and the material constants of the Mooney-Rivlin law of the vascular walls was also presented in Oliveira *et al.* (2022) and, for reference, was labelled as the "uniform-wall model" in that work due to its context. Nevertheless, they deserve further comments here. These properties were modelled with a globally heterogeneous model over the whole vasculature by computing different thicknesses and material constants on the branches and the aneurysm sac. This modelling was chosen to eliminate the local influence of the thickness and material constant heterogeneity on the mechanical response of the aneurysm sac — it is known that IA walls are heterogenous (Kadasi *et al.*, 2013) — while using a sufficiently realistic model of the walls.

Briefly, first the thickness of the branches (symbolically represented as S_b) was computed based on established evidence that the thickness of arteries is proportional to their lumen diameter (Fung, 1993). Then, based on the thickness field of the surrounding branches, we estimated the patient-specific uniform thickness of the IA sac surface (S_{ia}) as a weighted average of it (see the left panel of Fig. 1). This thickness field was then used to create the solid wall meshes.

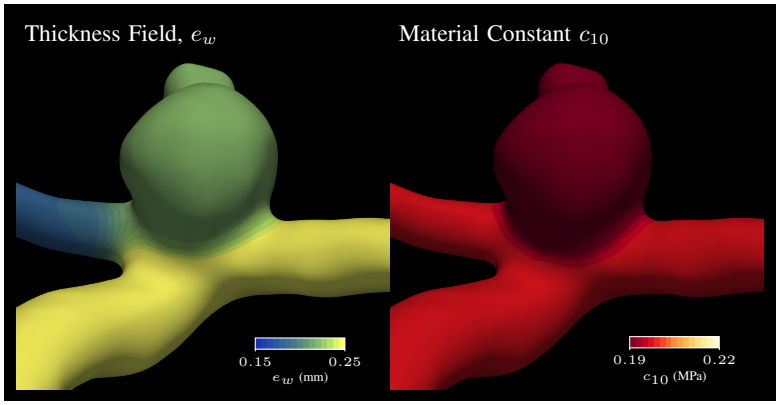

Figure 1. Example of the resulting thickness and material constant c_{10} fields defined *a priori* for IA case rICA2.

We assumed the material constants of the Mooney-Rivlin law, c_{10}, c_{01}, and c_{11}, as uniform in both the branches and aneurysm sac but with different values according to rupture status, following experimental evidence that unruptured IA tissue is stiffer than ruptured IA tissue (Costalat *et al.*, 2011). Hence, the values for each constant (see Table 1) were based on averages of experimental data, with ruptured and unruptured IAs, provided by Costalat *et al.* (2011). Regarding the material constants on S_b, we used the mean values of the entire samples measured by (Costalat *et al.*, 2011). This approach was preferred instead of using data from different studies and resulted in the material of the surrounding branches (i.e. healthy arteries) being less stiff than unruptured IAs, as suggested by experimental investigations (Robertson *et al.*, 2015).

Computationally, the heterogeneous fields of e_w and the three material constants were built with scripts in VMTK® and an in-house code based on the Visualization Toolkit (VTK)® (Oliveira, 2022). Figure 1 (right panel) shows an example of the resulting fields of wall thickness and the material constants c_{10} for case rICA2.

2.4 Computational Strategies

The numerical solution of Eqs. (1), (2) and (5) were computed using solids4foam (Cardiff *et al.*, 2018), compiled with the foam-extend library (foam-extend Project, 2017; Weller *et al.*, 1998), version 4.0 and all the details about the discretisation techniques that we employed can be found in Oliveira *et al.* (2022), including mesh and time-step independence tests with the same geometries used here.

Table 1. Material constants selected for arteries branches, S_b, and the IA sac, S_{ia}, according to rupture status based on the experimental work of Costalat *et al.* (2011).

Constant	S_b	S_{ia}	
		Ruptured	Unruptured
c_{10} (MPa)	0.1966	0.19	0.19
c_{01} (MPa)	0.0163	0.026	0.023
c_{11} (MPa)	7.837	1.377	11.780

2.5 Data Analysis

We analyzed the fields of the largest principal Cauchy stress, σ_1, and largest principal stretch, λ_1. All the results were taken on the inner surface of the vasculature (the so-called lumen) and at the peak systole instant, t_{ps}, and the results are shown in the reference configuration. The analysis performed used the absolute maximum to quantify σ_1 and λ_1 over the wall sac surface, S_{ia}, as given by:

$$(\sigma_1)_{max} = \max_{\boldsymbol{x}\in S_{ia}} \sigma_1(\boldsymbol{x})\,, \tag{8}$$

$$(\lambda_1)_{max} = \max_{\boldsymbol{x}\in S_{ia}} \lambda_1(\boldsymbol{x})\,, \tag{9}$$

because the largest stress and stretch potentially indicate the cases at the highest risk of rupture. We also analyzed the aneurysmal pulsatility, labeled here as δ_v, as defined by Sanchez *et al.* (2014) as:

$$\delta_v = \frac{V_{ps} - V_{ld}}{V_{ld}}\,, \tag{10}$$

where V_{ps} and V_{ld} are the luminal volume at the peak systole and low diastole, respectively.

3. RESULTS AND DISCUSSIONS

Figure 2 shows the distributions of $(\sigma_1)_{max}$ and $(\lambda_1)_{max}$ per rupture-status groups. We see an evident separation of $\langle\lambda_1\rangle$ between the two groups, although the same did not occur for $\langle\sigma_1\rangle$. The maximum σ_1 is not significantly different between ruptured and unruptured groups ($p = 0.42$), although the contrary is true for the maximum λ_1 ($p = 0.037$). Furthermore, note that the unruptured group not only accounts with individual data points for which $(\sigma_1)_{max}$ are larger than the ruptured group (indicated by the whiskers of the box-plots), but also both the distributions means and medians are higher in the unruptured group. This is somewhat counter intuitive because higher stress have always been associated with increased risk of tissue failure.

The results then suggest that λ_1 is more likely to play a role as a rupture-indicator. This is not entirely surprising because the less stiff properties assumed for the ruptured IAs would evidently cause larger deformations in this group compared with the unruptured one. The biggest surprise is that the same behavior was not found with the stresses, i.e. σ_1 is less likely to act as a potential rupture-indicator or to indicate whether particular cases of IAs are imminently closer to rupture. More importantly, the maximum stress was, on average, higher in unruptured IAs than ruptured ones. To the authors' knowledge, this has not been reported elsewhere in the literature in studies with a relatively large sample, only scarce data with only few aneurysms such as the numerical results provided by Lee *et al.* (2013). The authors conducted an FSI numerical study and found one unruptured case that had higher effective stress — their IA sample was relatively smaller, with two ruptured and three unruptured IAs. Finally, it is not prudent, though, to also conclude that stresses do not *cause* the rupture. Comprehensively, stress has been classically targeted as the variable that also explains soft tissue failure, thus possibly explaining the rupture of IAs, although it is known that the *normal* component of the stress is more important in this respect (Humphrey and Canham, 2000), in contrast to classical metal theories where shearing-based effective stresses, such as the von Mises stress, are used.

That the deformations are higher in ruptured aneurysms was also supported by simulations performed by Sanchez *et al.* (2014), who reported that aneurysmal pulsatility (Eq. (10)) is a potential predictor of IA rupture. The pulsatility calculated for the sample used in this work and its distribution are shown in Fig. 3. Clearly, δ_v follows the same trend that λ_1. Moreover, the average pulsatility of ruptured cases was significantly higher than that of unruptured cases ($p = 0.027$). Therefore, and in turn, the sample used in this work further support the results of Sanchez *et al.* (2014).

The aneurysmal pulsatility is a measure of the volumetric deformation of an IA sac, hence it depends on the deformation of the wall. The same is true of the largest principal stretch and other strain measures, rigorously, because they all

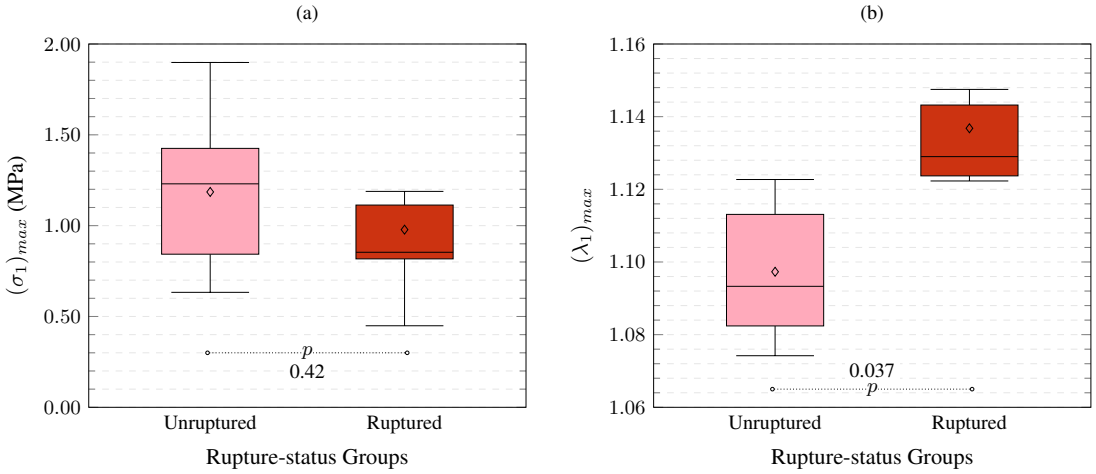

Figure 2. Distributions of (a) $(\sigma_1)_{max}$ and (b) $(\lambda_1)_{max}$ segregated by rupture-status groups (using box-plots to show the distributions: the box delimits the 25th and 75th percentiles, the middle bar indicates the distribution's mean and the diamond shape the median).

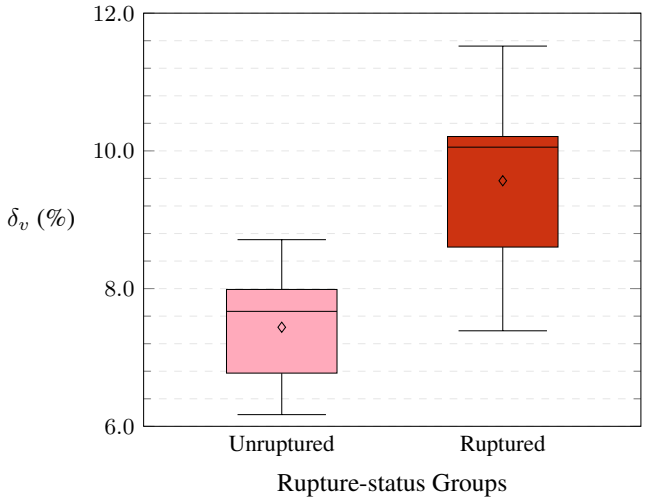

Figure 3. Box-plot of the distributions of δ_v for the IA sample segregated by rupture-status groups (using box-plots to show the distributions: the box delimits the 25th and 75th percentiles, the middle bar indicates the distribution's mean and the diamond shape the median).

ultimately depend on the wall displacement, $\boldsymbol{u}$. Therefore, the trends found for λ_1 and δ_v are physically related. Still, δ_v is easier to calculate for a single aneurysm case, as Sanchez *et al.* (2014) promptly pointed out, than $(\lambda_1)_{max}$, or any other metric of it, since the latter would depend on the whole λ_1 field.

An assessment of rupture likelihood based on the mechanical response computed for this work is not entirely complete without considering the failure properties of IAs tissue. Robertson *et al.* (2015) measured the ultimate Cauchy stress of IAs samples and found a mean of 1.39 MPa. Thus, based on the plots of Fig. 2, the unruptured group contains cases that would be effectively closer to rupture than the ruptured group. The large variability of the disease is what possibly explain, then, this seemingly confounding role of the stress. Robertson *et al.* (2015) further divided their sample in "low strength" and "high strength" aneurysms with a mean ultimate Cauchy stress of 0.68 ± 0.08 MPa and of 1.60 ± 0.36 MPa, respectively. High-strength tissue was more prevalent in their sample, hence the unruptured cases here could be all high-strength cases, whereas the ruptured ones could be all low-strength cases.

Additionally, Robertson *et al.* (2015) also measured the ultimate stretch of their sample and found an average of 1.31. Similarly, Brunel *et al.* (2018), who experimentally investigated the failure properties of IA tissue, reported an average ultimate stretch of 1.190 ± 0.069 and 1.210 ± 0.071 for ruptured and unruptured groups, respectively. By also considering the variability of the disease, these values could roughly explain the ruptured cases in the sample used here (see Fig. 2b). Interestingly, Brunel *et al.* (2018) also found a more consistent ultimate strain limit, of about $20.0 \pm 6.0\,\%$ of uniaxial deformation, than an ultimate stress limit, of about 0.38 ± 0.24 MPa of uniaxial engineering stress, for their sample. The

authors concluded that a "notion of strain limit is more relevant than one of stress limit". They highlight, though, that this was true only for the strain, instead of stretch. In the triaxial case, principal stretch and principal strains are related through a non-linear relationship given by $E_i = \lambda_i^2 - 1, i = 1, 2, 3$ (where here the principal values of the Green-Lagrange strain tensor, E_i, were employed). Their values were also estimated for the sample used in this work and, regardless, the strain measurements were still significantly higher for ruptured compared to unruptured aneurysms.

Ultimately, our results shed light on the relative complexity of an IA wall regarding its failure properties because, not only the inter-aneurysm variability is important, but it is most likely that the failure limits also vary spatially on an aneurysm sac. Therefore, more detailed data of the failure properties of IAs tissue is necessary for further assessment of the likelihood of rupture based on the mechanical response of a patient-specific IA. But determining both ultimate stress and ultimate stretch of a patient-specific aneurysm is currently almost impossible without invasive techniques and, probably, much more difficult than to obtain its thickness and material constants distributions over an aneurysm sac wall. Nevertheless, the fact that the stretch plays a more prominent role as an indicator of the rupture of an IA may also indicate that it could be an important physical variable related to the mechanisms behind the rupture event, i.e. it could point to the regions of an IA wall that are in danger.

4. CONCLUSIONS

Ruptured IAs had a significantly higher maximum stretch compared to unruptured ones, whereas the stress levels were not significantly different between the two groups — although, surprisingly, the stress levels were slightly higher on unruptured aneurysms. This indicates that deformation-related properties of the wall may indicate rupture. This is directly important to the medical practice and it suggests at looking on displacements, strains, and stretch patterns for qualitative assessments of the likelihood of rupture. This may become possible with time-resolved three-dimensional (3D) imaging techniques, such as four-dimensional (4D) computational tomography angiography (CTA), that were recently used to measure the displacement and pulsatility of IAs walls *in-vivo* (Zhang *et al.*, 2009; Ferrari *et al.*, 2019). Therefore, this could lead to assessing the likelihood of rupture from these examinations, as they become more common in the medical practice.

5. ACKNOWLEDGEMENTS

We are more than thankful to Prof. Dr. Julio Militzer (in memoriam), Dalhousie University, who participated actively in all the steps to accomplish this work. This research was supported by resources supplied by the Center for Scientific Computing (NCC/GridUNESP) of the São Paulo State University (UNESP) (`www2.unesp.br/portal#!/gridunesp`), by ACENET (`www.ace-net.ca`) through Dalhousie University and Digital Research Alliance of Canada (`https://alliancecan.ca/en`). Funding: This research was supported by grants 2017/18514-1, 2019/19098-7, and 2023/12122-5 of the São Paulo Research Foundation (FAPESP).

6. REFERENCES

Antiga, L., Ene-Iordache, B., Caverni, L., Cornalba, G.P. and Remuzzi, A., 2002. "Geometric reconstruction for computational mesh generation of arterial bifurcations from CT angiography". Vol. 26, pp. 227–235. URL `www.elsevier.com/locate/compmedimag`.

Antiga, L., Piccinelli, M., Botti, L., Ene-Iordache, B., Remuzzi, A. and Steinman, D.A., 2008. "An image-based modeling framework for patient-specific computational hemodynamics". Vol. 46, pp. 1097–1112. doi:10.1007/s11517-008-0420-1.

Bazilevs, Y., Hsu, M.C., Zhang, Y., Wang, W., Kvamsdal, T., Hentschel, S. and Isaksen, J.G., 2010. "Computational vascular fluid-structure interaction: Methodology and application to cerebral aneurysms". Vol. 9, pp. 481–498. ISSN 16177959. doi:10.1007/s10237-010-0189-7.

Brunel, H., Ambard, D., Dufour, H., Roche, P., Costalat, V. and Jourdan, F., 2018. "Rupture limit evaluation of human cerebral aneurysms wall: Experimental study". Vol. 77, pp. 76–82. ISSN 00219290. doi:10.1016/j.jbiomech.2018.06.016.

Cardiff, P., Karač, A., De Jaeger, P., Jasak, H., Nagy, J., Ivanković, A. and Tuković, v., 2018. "An open-source finite volume toolbox for solid mechanics and fluid-solid interaction simulations". URL `http://arxiv.org/abs/1808.10736`.

Cebral, J.R. and Meng, H., 2012. "Counterpoint: Realizing the Clinical Utility of Computational Fluid Dynamics—Closing the Gap". pp. 397–398. doi:10.3174/ajnr.a2993.

Chnafa, X.C., Brina, X.O., Pereira, V.M. and Steinman, X.D.A., 2018. "Better Than Nothing: A Rational Approach for Minimizing the Impact of Outflow Strategy on Cerebrovascular Simulations". Vol. 39, pp. 337–343. doi:10.3174/ajnr.A5484.

Costalat, V., Sanchez, M., Ambard, D., Thines, L., Lonjon, N., Nicoud, F., Brunel, H., Lejeune, J.P., Dufour, H., Bouillot, P., Lhaldky, J.P., Kouri, K., Segnarbieux, F., Maurage, C.A., Lobotesis, K., Villa-Uriol, M.C., Zhang, C., Frangi, A.F., Mercier, G., Bonafé, A., Sarry, L. and Jourdan, F., 2011. "Biomechanical wall properties of human intracranial aneurysms resected following surgical clipping (IRRAs Project)". Vol. 44, No. 15, pp. 2685–2691. doi:10.1016/j.jbiomech.2011.07.026.

Ferrari, F., Cirillo, L., Calbucci, F., Bartiromo, F., Ambrosetto, P., Fioravanti, A. and Leonardi, M., 2019. "Wall motion at 4D-CT angiography and surgical correlation in unruptured intracranial aneurysms: A pilot study". Vol. 63, No. 5. ISSN 03905616, 18271855. doi:10.23736/S0390-5616.16.03640-7.

foam-extend Project, 2017. "foam-extend Website". `https://sourceforge.net/projects/foam-extend/`. [Accessed 19-June-2017].

Fung, Y.C., Fronek, K. and Patitucci, P., 1979. "Pseudoelasticity of arteries and the choice of its mathematical expression". Vol. 237, No. 5, pp. H620–H631. ISSN 0002-9513. doi:10.1152/ajpheart.1979.237.5.H620.

Fung, Y.C., 1993. *Biomechanics - Mechanical Properties of Living Tissues*. Springer New York. ISBN 978-1-4419-3104-7 978-1-4757-2257-4. doi:10.1007/978-1-4757-2257-4.

Hirschhorn, M., Tchantchaleishvili, V., Stevens, R., Rossano, J. and Throckmorton, A., 2020. "Fluid–structure interaction modeling in cardiovascular medicine – A systematic review 2017–2019". Vol. 78, pp. 1–13. ISSN 13504533. doi:10.1016/j.medengphy.2020.01.008.

Hoi, Y., Wasserman, B.A., Xie, Y.J., Najjar, S.S., Ferruci, L., Lakatta, E.G., Gerstenblith, G. and Steinman, D.A., 2010. "Characterization of volumetric flow rate waveforms at the carotid bifurcations of older adults". Vol. 31, No. 3, pp. 291–302. ISSN 09673334. doi:10.1088/0967-3334/31/3/002.

Holzapfel, G.A., 2000. *Nonlinear Solid Mechanics*. John Wiley & Sons, Inc.

Holzapfel, G.A., Gasser, T.C. and Ogden, R.W., 2000. "A new constitutive framework for arterial wall mechanics and a comparative study of material models". Vol. 61, No. 1-3, pp. 1–48. ISSN 03743535. doi:10.1023/A:1010835316564.

Humphrey, J.D. and Canham, P.B., 2000. "Structure, Mechanical Properties, and Mechanics of Intracranial Saccular Aneurysms". Vol. 61, pp. 49–81.

Kadasi, L.M., Dent, W.C. and Malek, A.M., 2013. "Colocalization of thin-walled dome regions with low hemodynamic wall shear stress in unruptured cerebral aneurysms". Vol. 119, No. 1, pp. 172–179. ISSN 0022-3085. doi:10.3171/2013.2.jns12968.

Kallmes, D.F., 2012. "Point: CFD—Computational Fluid Dynamics or Confounding Factor Dissemination". Vol. 33, pp. 393–398. doi:10.3174/ajnr.A2993.

Kanyanta, V., 2009. "Towards early diagnosis of atherosclerosis: Accurate prediction of wall shear stress".

Lee, C.J., Zhang, Y., Takao, H., Murayama, Y. and Qian, Y., 2013. "A fluid-structure interaction study using patient-specific ruptured and unruptured aneurysm: The effect of aneurysm morphology, hypertension and elasticity". Vol. 46, No. 14, pp. 2402–2410. ISSN 00219290. doi:10.1016/j.jbiomech.2013.07.016.

Liang, L., Steinman, D.A., Brina, O., Chnafa, C., Cancelliere, N.M. and Pereira, V.M., 2019. "Towards the Clinical utility of CFD for assessment of intracranial aneurysm rupture - A systematic review and novel parameter-ranking tool". Vol. 11, pp. 153–158. ISSN 17598486. doi:10.1136/neurintsurg-2018-014246.

Mooney, M., 1940. "A Theory of Large Elastic Deformation". Vol. 11, No. 153. doi:10.1063/1.1713863.

Oliveira, I.L., 2022. "iagolessa/vmtk4aneurysms: Release version 1.0.0". doi:10.5281/zenodo.6675879. URL `https://doi.org/10.5281/zenodo.6675879`.

Oliveira, I., Cardiff, P., Baccin, C. and Gasche, J., 2022. "A numerical investigation of the mechanics of intracranial aneurysms walls: Assessing the influence of tissue hyperelastic laws and heterogeneous properties on the stress and stretch fields". Vol. 136, p. 105498. ISSN 17516161. doi:10.1016/j.jmbbm.2022.105498.

Passerini, T. and Piccinelli, M. and Veneziani, A. and Antiga, L., 2021. "aneurisk". `http://ecm2.mathcs.emory.edu/aneuriskweb/index`.

Piccinelli, M., Veneziani, A., Steinman, D.A., Remuzzi, A. and Antiga, L., 2009. "A framework for geometric analysis of vascular structures: Application to cerebral aneurysms". Vol. 28, No. 8, pp. 1141–1155. doi:10.1109/TMI.2009.2021652.

Robertson, A.M., Duan, X., Aziz, K.M., Hill, M.R., Watkins, S.C. and Cebral, J.R., 2015. "Diversity in the Strength and Structure of Unruptured Cerebral Aneurysms". Vol. 43, No. 7, pp. 1502–1515. doi:10.1007/s10439-015-1252-4.

Sacks, A.H. and Tickner, E.G., 1968. "The compressibility of blood". Vol. 5, No. 4, pp. 271–274. ISSN 18785034, 0006355X. doi:10.3233/BIR-1968-5403.

Sanchez, M., Ecker, O., Ambard, D., Jourdan, F., Nicoud, F., Mendez, S., Lejeune, J.P., Thines, L., Dufour, H., Brunel, H., Machi, P., Lobotesis, K., Bonafe, A. and Costalat, V., 2014. "Intracranial aneurysmal pulsatility as a new individual criterion for rupture risk evaluation: Biomechanical and numeric approach (IRRAs Project)". Vol. 35, pp. 1765–1771. doi:10.3174/ajnr.A3949.

Saqr, K.M., Rashad, S., Tupin, S., Niizuma, K., Hassan, T., Tominaga, T. and Ohta, M., 2019. "What does computational fluid dynamics tell us about intracranial aneurysms? A meta-analysis and critical review". Vol. 0, No. 0, pp. 1–19.

doi:10.1177/0271678X19854640.

Valencia, A., Burdiles, P., Ignat, M., Mura, J., Bravo, E., Rivera, R. and Sordo, J., 2013. "Fluid structural analysis of human cerebral aneurysm using their own wall mechanical properties". Vol. 2013, pp. 1–18. ISSN 1748670X. doi:10.1155/2013/293128.

Vlak, M.H.M., Rinkel, G.J.E., Greebe, P. and Algra, A., 2013. "Risk of rupture of an intracranial aneurysm based on patient characteristics: A case-control study". Vol. 44, No. 5, pp. 1256–1259. ISSN 00392499. doi:10.1161/STROKEAHA.111.000679.

VMTK, 2022. "VMTK Website". `http://www.vmtk.org/`. [Accessed 19-June-2022].

Weller, H.G., Tabor, G., Jasak, H. and Fureby, C., 1998. "A tensorial approach to computational continuum mechanics using object-oriented techniques". Vol. 12, pp. 620–631.

Zhang, C., Villa-Uriol, M.C., De Craene, M., Pozo, J. and Frangi, A., 2009. "Morphodynamic Analysis of Cerebral Aneurysm Pulsation From Time-Resolved Rotational Angiography". Vol. 28, No. 7, pp. 1105–1116. ISSN 0278-0062, 1558-254X. doi:10.1109/TMI.2009.2012405.

7. RESPONSIBILITY NOTICE

The authors are solely responsible for the printed material included in this paper.